1

Effects of Optical Interference and Annealing on the Performance of Polymer/Fullerene Bulk Heterojunction Solar Cells

Chunfu Zhang[1], Hailong You[1], Yue Hao[1],
Zhenhua Lin[2] and Chunxiang Zhu[2]
[1]*School Of Microelectronics, Xidian University,*
[2]*ECE, National University of Singapore,*
[1]*China*
[2]*Singapore*

1. Introduction

Polymer solar cells are of tremendous interests due to their attractive properties such as flexibility, ease of fabrication, low materials and energy budget. However, organic materials have short exciton diffusion length and poor charge mobility, which can greatly decrease the performance of polymer solar cells. These challenges can be effectively overcome through the use of the bulk heterojunction (HJ) structure because it can guarantee the effective exciton dissociation and carrier transport simultaneously if a proper bicontinuous interpenetrating network is formed in the active layer. Based on this structure, the performance of polymer solar cells has been improved steadily in the past decade.

The performance of a polymer solar cell is mainly determined by the short-circuit current density (J_{SC}), the open circuit voltage (V_{OC}), and the fill factor (*FF*), given that $\eta=J_{SC}V_{OC}FF/P_{in}$ (where η is power conversion efficiency, *PCE*, and P_{in} is the incident optical power density). V_{OC} has a direct relationship with the offset energies between the highest occupied molecular orbital of Donor (*D*) material and the lowest unoccupied molecular orbital of Acceptor (*A*) material (Cheyns et al., 2008). Since the *D* and *A* materials are intimately mixed together in the bulk HJ structure and their interfaces distribute everywhere in the active layer, it is difficult to increase V_{OC} by changing *D*/*A* interface property for a given material system (such as poly(3-hexylthiophene-2,5-diyl):[6,6]-phenyl C_{61} butyric acid methyl ester, P3HT:PCBM). Thus the usually used optimization method is to improve J_{SC} and *FF*.

J_{SC} greatly depends on the optical interference effect in polymer solar cells. Because of the very high optical absorption ability of organic materials, the active layer is very thin and typically from several ten to several hundred nanometers. This thickness is so thin compared to the incident light wavelength that the optical interference effect has to be carefully considered. Depending on the thicknesses and optical constants of the materials, the optical interference causes distinct distributions of the electric field and energy absorption density. Due to this effect, J_{SC} shows an obvious oscillatory behavior with the variation of active layer thickness. In order to gain a high *PCE*, the active layer thickness needs to be well optimized according to the optical interference.

Besides the serious optical interference effect, J_{SC} also suffers from the non-ideal free carrier generation, low mobility and short carrier lifetime. In order to reduce the exciton loss and guarantee the efficient carrier transport, the optimal interpenetrating network, or to say, the optimal morphology is desired in the bulk HJ structure. In order to achieve an optimal morphology, a thermal treatment is usually utilized in the device fabrication, especially for the widely used P3HT:PCBM solar devices. It is found that the sequence of the thermal treatment is critical for the device performance (Zhang et al., 2011). The polymer solar cells with the cathode confinement in the thermal treatment (post-annealed) show better performance than the solar cells without the cathode confinement in the thermal treatment (pre-annealed). The functions of the cathode confinement are investigated in this chapter by using X-ray photoelectron spectroscopy (XPS), atomic force microscopy (AFM), optical absorption analysis, and X-ray diffraction (XRD) analysis. It is found that the cathode confinement in the thermal treatment strengthens the contact between the active layer and the cathode by forming Al–O–C bonds and P3HT-Al complexes. The improved contact effectively improves the device charge collection ability. More importantly, it is found that the cathode confinement in the thermal treatment greatly improves the active layer morphology. The capped cathode effectively prevents the overgrowth of the PCBM molecules and, at the same time, increases the crystallization of P3HT during the thermal treatment. Thus, a better bicontinuous interpenetrating network is formed, which greatly reduces the exciton loss and improves the charge transport capability. Meanwhile, the enhanced crystallites of P3HT improve the absorption property of the active layer. All these aforementioned effects together can lead to the great performance improvement of polymer solar cells. Besides the thermal treatment sequence, temperature is another very important parameter in the annealing process. Various annealing temperatures have also been tested to find the optimized annealing condition in this chapter.

The contents of this chapter are arranged as the following: Section 2 introduces the effects of the optical interference on J_{SC} in polymer solar cells by considering the non-ideal free carrier generation, low mobility and short carrier lifetime at the same time; Section 3 investigates the influence of the sequence of the thermal treatment on the device performance with emphasis on the cathode confinement in the thermal treatment; based on the optical interference study and the proper thermal treatment sequence, the overall device optimization is presented in Section 4. At last, a short conclusion is given in Section 5.

2. Effects of optical interference on J_{SC}

J_{SC} is directly related to the absorption ability of organic materials. It is believed that increasing the light harvesting ability of the active layer is an effective method to increase J_{SC}. In order to increase J_{SC}, some optical models (Pettersson, 1999; Peumans et al., 2003) have been built to optimize the active layer thickness. However, only optimizing the thickness for better light absorption is difficult to improve J_{SC}. This is because that *PCE* depends not only on the light absorption, but also on exciton dissociation and charge collection. In polymer solar cells, a blend layer consisting of conjugated polymer as the electron donor and fullerene as the electron acceptor is always used as the active layer. For a well blended layer, the length scale of *D* and *A* phases is smaller than the exciton diffusion length (typically less than 10 nm), so that most of the generated excitons can diffuse to the *D/A* interface before they decay. Even if all the excitons can reach the *D/A* interface, not all of them can be dissociated into free carriers. The exciton-to-free-carrier

dissociation probability is not 1 and depends on some factors such as electric field and temperature. When the active layer thickness is increased to optimize the light absorption, the electric field in the blend layer decreases, which lowers down the exciton-to-free-carrier probability and makes charge collection less effective simultaneously. As a result, J_{SC} may become low, although the thickness has been optimized for better light absorption. Thus to obtain a higher J_{SC}, both the optical and the electric properties should be considered at the same time.

Some previous works (Lacic et al., 2005; Monestier et al., 2007) studied the characteristic of J_{SC}. However, they neglected the influence of exciton-to-free-carrier probability, which is important for polymer solar cells. Another study (Koster et al., 2005) considered this factor, but they neglected the optical interference effect, which is a basic property for the very thin organic film. All the above studies are based on the numerical method, and it is not easy to solve the equations and understand the direct influence of various parameters on J_{SC}. In this part, a model predicting J_{SC} is presented by using very simple analytical equations. Based on this model, the effects of optical interference on J_{SC} is investigated. Besides, the carrier lifetime is also found to be an important factor. By considering the optical interference effect and the the carrier lifetime, it is found that when the lifetimes of both electrons and holes are long enough, the exciton-to-free-carrier dissociation probability plays a very important role for a thick active layer and J_{SC} behaves wavelike with the variation of the active layer thickness; when the lifetime of one type of carrier is too short, the accumulation of charges appears near the electrode and J_{SC} increases at the initial stage and then decreases rapidly with the increase of the active layer thickness.

2.1 Theory

2.1.1 Exciton generation

The active layer in polymer solar cells absorbs the light energy when it is propagating through this layer. How much energy can be absorbed depends on the complex index of refraction $\bar{n} = n + i\kappa$ of the materials. At the position z in the organic film (Fig. 1 (a)), the time average of the energy dissipated per second for a given wavelength λ of incident light can be calculated by

$$Q(z,\lambda) = \frac{1}{2} c\varepsilon_0 \alpha_j n \left|\bar{E}(z)\right|^2 \tag{1}$$

where c is the vacuum speed of light, ε_0 the permittivity of vacuum, n the real index of refraction, α the absorption coefficient, $\alpha = 4\pi\kappa / \lambda$, and $E(z)$ the electrical optical field at point z. $Q(z,\lambda)$ have the unit of W / m^3 . Assuming that every photon generates one exciton, the exciton generation rate at position z in the material is given by

$$G(z,\lambda) = \frac{Q(z,\lambda)}{h\gamma} = \frac{\lambda}{hc} Q(z,\lambda) \tag{2}$$

where h is Planck constant, and γ is the frequency of incident light. The total excitons generated by the material at position z in solar spectrum are calculated by

$$G(z) = \int_{300}^{800} G(z,\lambda) d\lambda \tag{3}$$

Here the integration is performed from 300 nm to 800 nm, which is because that beyond this range, only very weak light can be absorbed by P3HT: PCBM active layer. In inorganic solar cells, $Q(z,\lambda)$ is usually modeled by

$$Q(z,\lambda) = \alpha I_0 e^{-\alpha z} \tag{4}$$

I_0 is the incident light intensity. Here, the optical interference effect of the materials is neglected. But in polymer solar cells, the active layers are so thin compared to the wavelength that the optical interference effect cannot be neglected.

2.1.2 Optical model

In order to obtain the distribution of electromagnetic field in a multilayer structure, the optical transfer-matrix theory (TMF) is one of the most elegant methods. In this method, the light is treated as a propagating plane wave, which is transmitted and reflected on the interface. As shown in Fig. 1 (a), a polymer solar cell usually consists of a stack of several layers. Each layer can be treated to be smooth, homogenous and described by the same complex index of refraction $\bar{n} = n + i\kappa$. The optical electric field at any position in the stack is decomposed into two parts: an upstream component E^+ and a downstream component E^-, as shown in Fig. 1 (a). According to Fresnel theory, the complex reflection and transmission coefficients for a propagating plane wave along the surface normal between two adjacent layers *j* and *k* are

$$r_{jk} = \frac{\overline{n_j} - \overline{n_k}}{\overline{n_j} + \overline{n_k}} \tag{5a}$$

$$t_{jk} = \frac{2\overline{n_j}}{\overline{n_j} + \overline{n_k}} \tag{5b}$$

where r_{jk} and t_{jk} are the reflection coefficient and the transmission coefficient, $\overline{n_j}$ and $\overline{n_k}$ the complex index of refraction for layer *j* and layer *k*. So the interface matrix between the two adjacent layers is simply described as

$$I_{jk} = \frac{1}{t_{jk}}\begin{bmatrix} 1 & r_{jk} \\ r_{jk} & 1 \end{bmatrix} = \begin{bmatrix} \dfrac{\overline{n_j} + \overline{n_k}}{2\overline{n_j}} & \dfrac{\overline{n_j} - \overline{n_k}}{2\overline{n_j}} \\ \dfrac{\overline{n_j} - \overline{n_k}}{2\overline{n_j}} & \dfrac{\overline{n_j} + \overline{n_k}}{2\overline{n_j}} \end{bmatrix} \tag{6}$$

When light travels in layer *j* with the thickness *d*, the phase change can be described by the layer matrix (phase matrix)

$$L_j = \begin{bmatrix} e^{-i\beta_j} & 0 \\ 0 & e^{i\beta_j} \end{bmatrix} \tag{7}$$

where $\beta_j = 2\pi\overline{n}_j d_j / \lambda$ is phase change the wave experiences as it traverses in layer *j*. The optical electric fields in the substrate (subscript *0*) and the final layer (subscript *m+1*) have the relationship as

$$\begin{bmatrix} \overline{E_0^+} \\ \overline{E_0^-} \end{bmatrix} = S \begin{bmatrix} \overline{E_{m+1}^+} \\ \overline{E_{m+1}^-} \end{bmatrix} = \begin{bmatrix} S_{11} & S_{12} \\ S_{12} & S_{22} \end{bmatrix} \begin{bmatrix} \overline{E_{m+1}^+} \\ \overline{E_{m+1}^-} \end{bmatrix} = \left(\prod_{v=1}^{m} I_{(v-1)v} L_v \right) \bullet I_{m(m+1)} \tag{8}$$

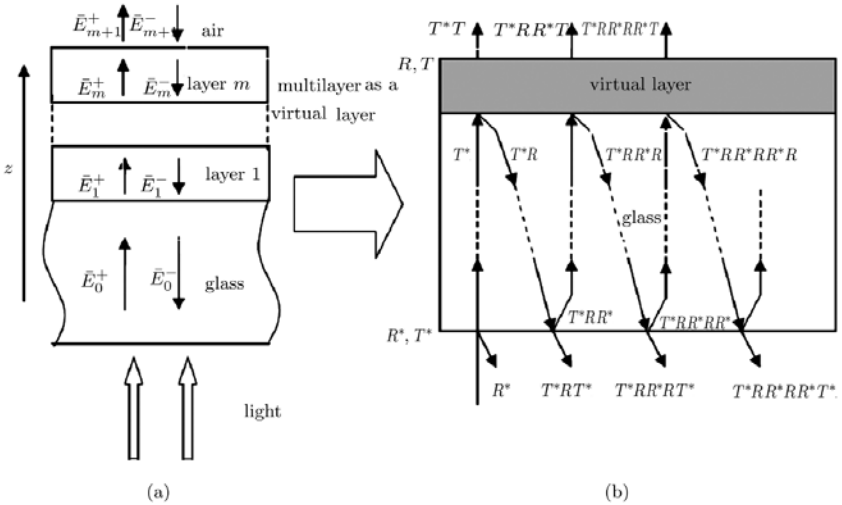

Fig. 1. Multilayer structure in a polymer solar cell. (a) the optical electric field in each layer and (b) treating the multilayer as a virtual layer.

Because in the final layer, $\overline{E_{m+1}^-}$ is 0, it can be derived that the complex reflection and transmission coefficients for the whole multilayer are:

$$r = \frac{\overline{E_0^-}}{\overline{E_0^+}} = \frac{S_{21}}{S_{11}} \tag{9a}$$

$$t = \frac{\overline{E_{m+1}^+}}{\overline{E_0^+}} = \frac{1}{S_{11}} \tag{9b}$$

In order to get the optical electric field E_j (z) in layer *j*, *S* is divided into two parts,

$$S = S_j^{'} L_j S_j^{''} \tag{10}$$

Where

$$S_j^{'} = \left(\prod_{v=1}^{j-1} I_{(v-1)v} L_v \right) \bullet I_{j(j-1)} \tag{11a}$$

$$S_j^{''} = \left(\prod_{v=j+1}^{m} I_{(v-1)v} L_v \right) \bullet I_{m(m+1)} \tag{11b}$$

At the down interface in layer *j*, the upstream optical electric field is denoted as

$$\overline{E_j^+} = t_j^+ \bullet \overline{E_0^+} = \frac{S_{j11}^{''}}{S_{j11}^{'} S_{j11}^{''} + S_{j12}^{'} S_{j21}^{''} e^{i2\beta_j}} \overline{E_0^+} \tag{12}$$

Similarly, at the up interface in layer *j*, the downstream optical electric field is

$$\overline{E_j^-} = t_j^- \bullet \overline{E_0^+} = \frac{S_{j21}^{''}}{S_{j11}^{''}} e^{i2\beta_j} \overline{E_j^+} \tag{13}$$

The optical electric field $\overline{E_j}(z)$ at any position z in layer j is the sum of upstream part $\overline{E_j^+}(z)$ and downstream part $\overline{E_j^-}(z)$

$$\overline{E_j}(z) = \overline{E_j^+}(z) + \overline{E_j^-}(z) = (t_j^+ e^{i\beta_j} + t_j^- e^{-i\beta_j}) \overline{E_0^+} \tag{14}$$

2.1.3 Light loss due to the substrate

Because the glass substrate is very thick compared to wavelength (usually 1mm>> wavelength), the optical interference effect in the substrate can be neglected. Here only the correction of the light intensity at the air/substrate and substrate/multilayer interfaces is made. As shown in Fig. 1 (b), the multilayer can be treated as a virtual layer whose complex reflection and transmission coefficients can be calculated using above equations. Then the irradiance to the multilayer is

$$I_g = T \left(\sum_{i=0}^{\infty} (R^* R)^i \right) I_0 = \frac{1 - R^*}{1 - RR^*} I_0 \tag{15}$$

I_g is described as

$$I_g = \frac{1}{2} c \varepsilon_0 n_g \left| E_0^+ \right|^2 \tag{16}$$

It can be derived that

$$\left| E_0^+ \right| = \sqrt{\frac{2(1 - R^*) * I_0}{\varepsilon_0 c n_g (1 - RR^*)}} \tag{17}$$

2.1.4 Free carrier generation

When the excitons are generated, not all of them can be dissociated into free carriers. The dissociation probability depends on the electric field and temperature. Recently, the

dissociation probability has been taken into consideration in polymer solar cells [13, 16]. The geminate recombination theory, first introduced by Onsager and refined by Brau later, gives the probability of electron-hole pair dissociation,

$$P(F,T) = \frac{k_D(F)}{k_D(F) + k_X} \tag{18}$$

where k_X is the decay rate to the ground state and k_D the dissociation rate of a bound pair. Braun gives the simplified form for dissociation rate

$$k_D(F) = k_R e^{-U_B/k_B T}\left[1 + b + \frac{b^2}{3} + \cdots\right] \tag{19}$$

where a is the initial separation distance of a given electron-hole pair, U_B is electron-hole pair binding energy described as $U_B = q^2/(4\pi\varepsilon_0\varepsilon_r a)$ and $b = q^3F/(8\pi\varepsilon_0\varepsilon_r k_B T^2)$. T is the temperature, F the electric field and ε_r the dielectric constant of the material. In equation (19), k_R is a function of the carrier recombination. For simplification, we treat k_R as a constant. Thus, the dissociation probability P only depends on the electric field F when the temperature keeps constant.

2.1.5 J_{SC} expression equations

J_{SC} is determined by the number of carriers collected by the electrodes in the period of their lifetime τ under short circuit condition. If the active layer thickness L is shorter than the electron and hole drift lengths (which is the product of carrier mobility μ, the electric field F and the carrier lifetime τ) or in other word, the lifetimes of both types of carriers exceed their transit time (case I as in Fig 2 (a)), all generated free carriers can be collected by the electrodes. Considering the exciton-to-free-carrier dissociation probability P, J_{SC} is

$$J_{SC} = qP(F,T)GL \tag{20}$$

where G is the average exciton generation rate in the active layer.

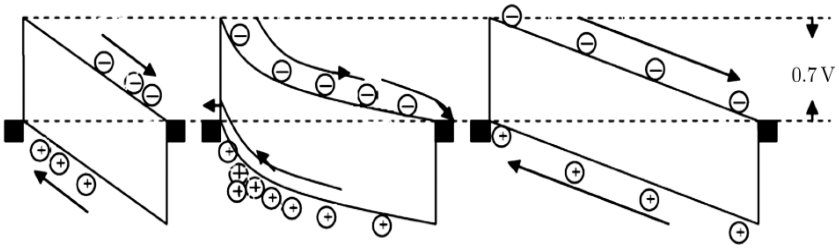

Fig. 2. Energy band diagrams under short circuit condition. (a) Case I: thickness is shorter than both drift lengths, (b) Case II: thickness is longer than hole drift length but shorter than electron drift length, c) Case III: thickness is longer than both hole and electron drift lengths.

If L is longer than drift lengths of electrons and holes, that is to say that the lifetimes of both types of carriers are smaller than their transit time, the carriers are accumulated in the active layer. At steady state, J_{SC} follows Ohm's law. Considering the exciton-to-free-carrier dissociation probability P, J_{SC} is

$$J_{SC} = qP(F,T)G(\mu_e\tau_e + \mu_h\tau_h)F = qP(F,T)G(\mu_e\tau_e + \mu_h\tau_h)V_{bi} / L \tag{21}$$

where V_{bi} is the built-in potential which is usually determined by the difference between cathode and anode work functions. This is case III as described in Fig. 2 (c).

Between case I and case III, it is case II as described in Fig. 2 (b). In this case, L is only longer than the drift length of one type of carrier. For P3HT:PCBM based polymer solar cells, the mobilities of holes and electrons in P3HT:PCBM (1:1 by weight) layer are $2\times10^{-8}\,m^2V^{-1}s^{-1}$ and $3\times10^{-7}\,m^2V^{-1}s^{-1}$, respectively [Mihailetchi et al., 2006]. Because the hole mobility is one order lower than the electron mobility, holes are easy to accumulate in the active layer, which makes the electric field non-uniform. In order to enhance the extraction of holes, the electric field increases near the anode. On the other hand, in order to diminish the extraction of electrons, the electric field decreases near the cathode. The electric field is modified until the extraction of holes equal to the extraction of electrons. Goodman and Rose studied this case and gave an equation for the photocurrent [Goodman & Rose, 1971]. Considering the exciton-to-free-carrier dissociation probability P, J_{SC} is

$$J_{sc} = qP(F,T)GL(1+c)\frac{-c + (c^2 + 4(1-c)V\mu_h\tau_h / L^2)^{\frac{1}{2}}}{2(1-c)} \tag{22}$$

where $c = \mu_h\tau_h / (\mu_e\tau_e)$ is the drift length ratio of holes and electrons. When $c<<1$, the equation is simplified to

$$J_{sc} = qP(F,T)G(\mu_h\tau_h)^{1/2}V^{1/2} \tag{23}$$

2.2 Results and discussion

2.2.1 Exciton generation profile in the active layer

For the studied bulk HJ cell, the D and A materials are well blended and form the active layer. Because the D and A domains are very small, we can neglect the complex reflection and transmission at D/A interfaces, and treat the whole active layer as one homogenous material. All the optical constants (n, k) of the indium tin oxide (ITO), poly(3, 4-ethylenedioxythiophene):poly (styrene sulfonate) (PEDOT:PSS), P3HT:PCBM and the Al electrode are input into our program, and the exciton generation rate in polymer solar cells is calculated. If the interference effect is neglected, the exciton generation rate decreases with the increasing thickness of the active layer as described in equation (4) which makes the corresponding average exciton generation rate (total exciton generation rate divided by the thickness) become smaller. However, when the optical interference effect is considered, the modulation effect of average exciton generation rate with the thickness variation is very clear as shown in Fig. 3. At the initial stage, the average exciton generation rate increases with the increasing thickness of the active layer. This is because the first light peak does not appear in the active layer when the active layer is thin due to the interference effect. With the increase of the active layer, the first light peak approaches and enters the active layer

such that the average generation rate becomes larger. With the further increase of the active layer, the average generation rate decreases although other light peaks enter the active layer. This is because for a thicker film, the thickness of the active layer dominates the generation rate. This evolution of exciton generation is plotted in Fig. 4 for the 500 nm wavelength.

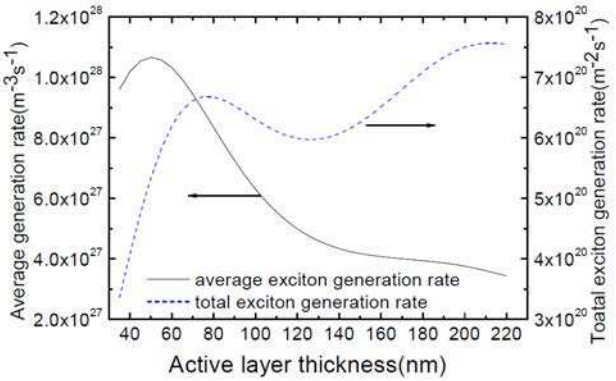

Fig. 3. The calculated exciton generation rate in the active layer when the optical interference effect is considered.

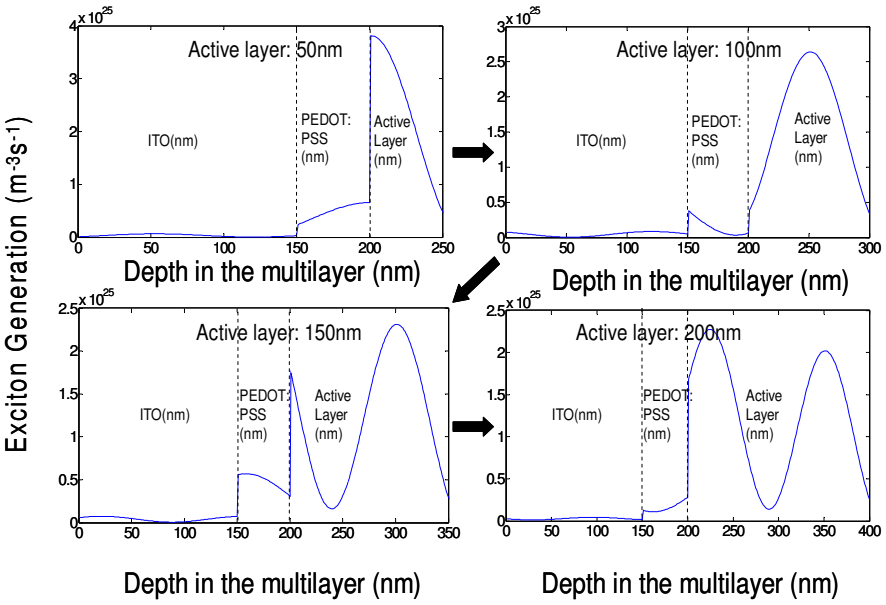

Fig. 4. Evolution of exciton generation in the active layer. The light wavelength is 500 nm. It can be seen that with the increase of the active layer thickness, the first peak enters the active layer, which makes the average exciton generation rate become large. For very thick film, although other peaks can enter the active layer, the absolute values for the peaks become small, which leads to the corresponding decrease of average exciton generation rate.

2.2.2 J_{SC} and the active layer thickness

Based on the calculated exciton generation rate, it is easy to predict J_{SC} when the drift lengths of both carriers are larger than the blend layer thickness. If all the generated excitons can be dissociated into free carriers, and then collected by the electrodes, J_{SC} should be proportional to the total exciton generation rate and behave wavelike as shown in Fig. 5 (solid line). Monestier [Monestier et al., 2007] have found this trend based on P3HT:PCBM systems. In their experiments, the active layer thickness is varied from a few tens nanometer to 215 nm. When the thickness is 70 nm, J_{SC} reaches the maximum value, and followed by a little decrease until 140 nm. When the thickness increases further, J_{SC} increases again. Unfortunately, there is obvious deviation between the prediction and the experiment results, especially in the thick film as shown in Fig. 5 (solid line). Obviously, the assumption that the exciton-to-free-carrier dissociation probability is unity is not correct. The influence of dissociation probability on J_{SC} must be considered.

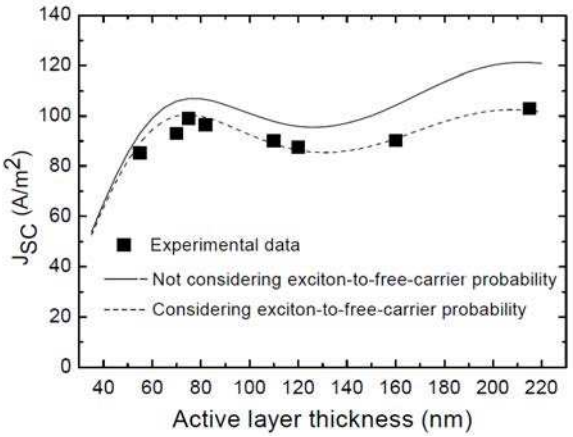

Fig. 5. Long carrier lifetime condition: the lifetimes of both carriers are always longer than their transient time. Experimental data are extracted from the work (Monestier et al. 2007).

In the previous work, Mihailetchi [Mihailetchi et al., 2006] exactly predicted photocurrent of P3HT:PCBM solar cells by assuming the same e-h separation distance (a) and decay rate (k_X). By fitting the experimental data, they obtained e-h separation distance of a=1.8 nm, room temperature bound pair decay rate of $k_X \approx 2\times10^4\,s^{-1}$ for a 120 nm active layer, and the dissociation probability is close to 90%. We use the same data and derive the parameter $k_R = 3.9662\times10^8\,S^{-1}$ (equation 19). The dissociation probability is calculated according to section 2.1.4. The results are shown in Fig. 6. Obviously, the exciton-to-free-carrier probability becomes lower with the increase of the active layer thickness. Using the results to correct J_{SC}, another J_{SC} curve is obtained and also shown in Fig. 5 (dash line). It can be seen that the predicted J_{SC} is exactly in accordance with the experimental results. This confirms the validity of our model. In the previous work, Monestier [Monestier et al., 2007]] modeled J_{SC} and found that the predicted J_{SC} is larger than the experimental data, especially for the thickness larger than 180 nm. They attributed this to the thickness dependence of optical constants. Here, according to our model, it is found that the deviation should come from the low exciton-to-free-carrier probability for thick active layers.

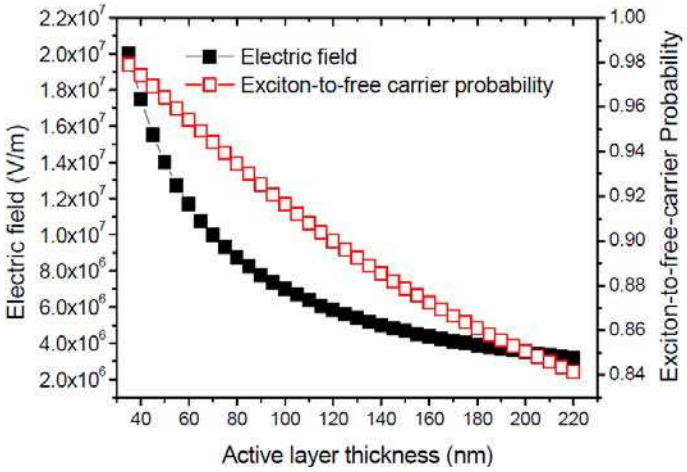

Fig. 6. Relations of electric field and exciton-to-free-carrier probability with layer thickness.

We have predicted J_{SC} precisely for the long enough carrier lifetime case. However, for polymer solar cells, the performance is sensitive to the process and experimental conditions. This may make the carrier lifetime relatively short. For P3HT:PCBM system, because the hole mobility is one order of magnitude lower than the electron mobility, holes are easy to accumulate in the active layer and limit the photocurrent. This is the case II as described in section 2.1.5. By tuning the parameters to fit the experimental data, the best fitting curve is obtained (Fig. 7) when the average hole lifetime τ is $6.2 \times 10^{-7} s$ and exciton-to-free-carrier dissociation probability is unity. A short lifetime τ may imply that there are many defects.

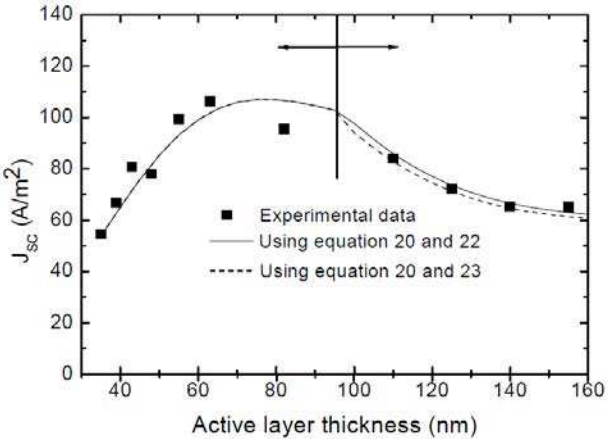

Fig. 7. Short hole carrier lifetime condition. Left arrow: hole lifetime is longer than its transient time; right arrow: hole lifetime is shorter than its transient time, and hole lifetime is $6.2 \times 10^{-7} s$, and electron lifetime is $1 \times 10^{-6} s$. Experimental data are from [Li et al., 2005].

These defects increase the exciton-to-free-carrier probability. More important, the transport process becomes the dominant limiting factor for J_{SC}, and the exciton-to-free-carrier process becomes relatively unimportant. Then it seems that the assumption of exciton-to-free-carrier probability as unity can satisfy the need of the prediction. In Fig. 7, we can see that there are two regions in the fitting curve. The left region is determined by equation (20). In this region, the lifetimes of both carriers are longer than their transient time. The solid line in the right region is determined by equation (22). In this region, hole lifetime is shorter than its transit time and electron lifetime is longer than its transit time.
If it is assumed that the drift length ratio of hole and electron is very small, then the equation (23) can be used to predict J_{SC}. As shown in Fig. 7 (dash line), it can predict J_{SC} very well, which means $c<<1$.

2.3 Summary

In this part, the exciton generation rate was calculated by taking the optical interference effect into account. Based on the calculated exciton generation rate, the dependence of J_{SC} on the active layer thickness was analyzed and compared with experimental data. Because of the optical interference effect, the total exciton generation rate does not monotonously increase with the increase of the active layer thickness, but behaves wavelike which induces the corresponding variation of J_{SC}. The carrier lifetimes also influence J_{SC} greatly. When the lifetimes of both electrons and holes are long enough, dissociation probability plays an important role for the thick active layer. J_{SC} behaves wavelike with the variation of the active layer thickness. When the hole lifetime is too short (drift length is smaller than device thickness), accumulation of charges appears near the electrode and J_{SC} increases at the initial stage and then decreases rapidly with the increase of the active layer thickness. The accordance between the predictions and the experimental results confirms the validity of the proposed model. These results give a guideline to optimize J_{SC}.

3. Effects of annealing sequence on J_{SC}

The detail of the interpenetrating network, or to say, the morphology is essentially important for the performance of polymer solar cells. In order to achieve an optimal morphology, a thermal treatment is usually utilized in the device fabrication. The thermal treatment can be carried out after and before the electrode deposition. Both the methods can greatly improve the device performance. The functions of the thermal treatment have been extensively investigated, and it has been shown that the morphology will be rearranged through the nanoscale phase separation between donor and acceptor components during the thermal treatment. By carefully optimizing the thermal treatment condition, an optimal interpenetrating network can be formed, which greatly improves the charge transport property. Besides, the thermal treatment can also effectively enhance the crystallization of P3HT, which will increase the hole mobility and the optical absorption capability. Due to the importance of the thermal treatment for P3HT:PCBM solar devices, great efforts have been devoted into the study of the thermal annealing process in the past few years. How the thermal annealing ambient, thermal annealing temperature and thermal annealing time affect the device performance has been well studied. However, only very few studies paid attention to the role of cathode in the thermal treatment. As is known, the thermal treatment can be done before and after the cathode deposition and both methods can greatly improve the device performance. The unique difference between them is whether there is cathode confinement in the thermal treatment or not. Although most of the previous studies have

tended to use the cathode confinement and carry out the thermal treatment after the cathode deposition, what are the functions of the cathode confinement in the thermal treatment and how they affect the device performance are still not well studied.
In this part, the effects of cathode confinement on the performance of polymer solar cells are investigated. It is shown that a better device performance can be achieved by using the cathode confinement in the thermal treatment. The experimental analysis indicates that by capping the cathode before the thermal treatment, the Al-O-C bonds and P3HT-Al complexes are formed at the interface between the P3HT:PCBM active layer and the cathode, which leads to a better contact and thus improves the charge collection capability. More importantly, the cathode confinement in the thermal treatment greatly improves the active layer morphology. It is shown that the cathode confinement in the thermal treatment can effectively inhibit the overgrowth of the PCBM molecules, and at the same time increase the crystallization of P3HT. Thus, a better morphology is achieved, which effectively reduces the exciton loss and improves the charge transport capability. Meanwhile, the enhanced P3HT crystallites improve the absorption property of the active layer. All these effects contribute to improve the device performance.

3.1 Experimental

Fig. 8 shows the layer structure of our polymer solar cells and the chemical structures of P3HT and PCBM. All the devices were fabricated on the ITO-coated glass substrates. Briefly, after being cleaned sequentially with detergent, de-ionized water, acetone, and isopropanol in an ultrasonic bath for about 15 mins, the dried ITO glass substrates were treated with oxygen plasma for about 3 mins. Then the filtered PEDOT:PSS (Baytron P VP AI 4083) suspension (through 0.45 μm filter) was spun coated on top of the ITO surface to form a ~50 nm layer under ambient condition, and dried at 120^{o}C in an oven for about one hour.

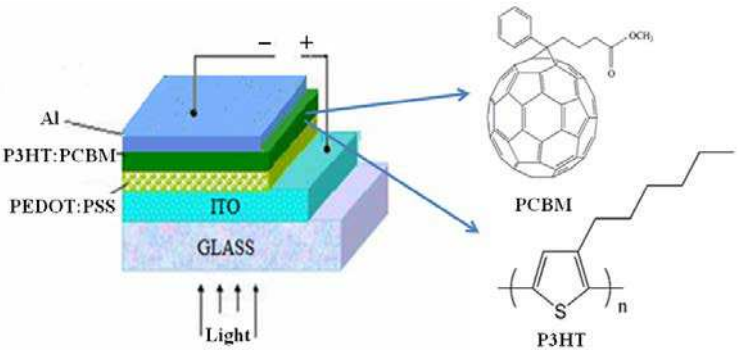

Fig. 8. Layer structure of the polymer solar cells investigated in this work.

P3HT:PCBM solution dissolved in 1,2-dichlorobenzene with a weight ratio of 1:0.8 was then spun coated on the PEDOT:PSS layer in the glove box to form a 100 nm blend layer. A 100 nm Al cathode was further thermally evaporated through a shadow mask giving an active device area of 20 mm^2. In order to investigate the effects of the cathode confinement on the device performance in the thermal treatment, two different types of devices were investigated: the devices without the cathode confinement in the thermal treatment (anneal the devices before the cathode deposition, pre-anneal) and the devices with the cathode confinement in the thermal treatment (anneal the devices after the cathode deposition, post-

anneal). The thermal treatment was carried out by annealing the devices in the glove box at the optimized temperature of 160 °C for about 10 mins as our previous report [Zhang et al., 2008]. For reference, the devices without any thermal treatment were also fabricated.
The current-voltage (*J-V*) characteristics were measured by a Keithley 2400 source-measure unit under AM 1.5 solar illumination at intensity of 100 mW/cm² calibrated by a Thorlabs optical power meter. The XPS samples were consisted of an identical sandwiched structure: ITO coated glass/P3HT:PCBM(100 nm)/Al (3 nm). Because XPS is a surface chemical analysis technique (top 1-10 nm usually), here only a very thin metal layer is used as others [39]. The XPS spectra were measured by transferring the samples to the chamber of a Kratos AXIS HSi spectrometer at once. The operating pressure of the analysis chamber was maintained at $8x10^{-9}$ Torr. A 1486.71 eV monochromatic Al Kα x-ray gun source was used to achieve the Al 2p, O 1s, C 1s and S 2p spectra. Tapping mode AFM measurements were taken with a Nanoscope III A (Digital Instruments) scanning probe microscope. The samples were prepared in the same sequence as the XPS samples. The phase images and the line scanning profiles of the samples were then recorded under air operation. For both the optical absorption study and x-ray diffraction measurement, the thin films of P3HT:PCBM in the same thickness of 100 nm were spun cast on the microscope slides. The optical absorption study was recorded by a Shimadzu UV-3101 PC UV-VIS-NIR scanning spectrophotometer. The XRD measurement was carried out by the θ-2θ scan method with CuKα radiation (λ = 0.1542 nm) using a Shimadu X-Ray diffractometer.

3.2 Results and discussion

Fig. 9 shows the *J-V* characteristics of the devices with the same configuration of ITO/PEDOT:PSS/P3HT:PCBM/Al. For the device without any thermal treatment, it shows the solar response with J_{SC} of 5.12 mA/cm², V_{OC} of 0.58 V, *FF* of 47.63% and *PCE* of 1.41%. The device performance is greatly improved by the thermal treatment. However, there are obvious differences for the devices with and without the cathode confinement in the thermal treatment as shown in Fig. 9 and Table 1. For the device without the cathode confinement in the thermal treatment, it shows the performance of J_{SC}=7.50 mA/cm², V_{OC}=0.58 V, *FF*=57.13% and *PCE*=2.49%. However, a further performance improvement is observed for the device with the cathode confinement in the thermal treatment, which shows a better performance of J_{SC}=8.34 mA/cm², V_{OC}=0.60 V, *FF*=62.57% and *PCE*=3.12%. It can be seen that the cathode confinement in the thermal treatment effectively increases J_{SC} and *FF*, which makes the overall *PCE* improved by 25%. This trend was found for a series of cells. Similar results are reported recently [Kim et al, 2009] where they also observed that the device with thermal treatment after cathode deposition could show a better performance. This further confirms our experimental results.

Samples	V_{OC}	J_{SC}	FF	PCE	J_0	J_{ph}	n	R_{sh}	R_s
Without thermal treatment	0.58	5.13	47.64	1.42	2.75e-4	5.32	2.32	778.25	29.00
Without cathode confinement	0.58	7.50	57.13	2.49	4.80e-5	7.62	1.89	575.19	9.34
With cathode confinement	0.60	8.34	62.25	3.12	3.03e-5	8.40	1.88	617.28	4.43

Units of parameters, V_{OC}: V; J_{SC}, J_0 and J_{ph}: mA/cm²; FF and PCE: %; $R_{sh}$and R_s: Ω cm².

Table 1. Summary of the Parameters Extracted from the J-V Curves Shown in Fig. 9

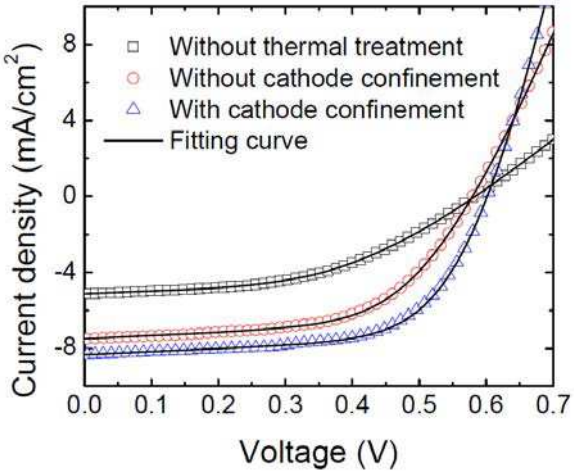

Fig. 9. *J-V* characteristics of the solar cells under the AM 1.5 illumination with the light intensity of 100 mW/cm². *T*he devices without (circle) and with (triangle) the cathode confinement in the thermal treatment and the device without any thermal treatment (squire) are shown in the graph. Solid lines are the fitting curves according to equation (24).

In order to understand the functions of the cathode confinement in the thermal treatment, the electrical parameters need to be extracted. The *J-V* characteristics of organic solar cells can be described approximated by the Shockley equation

$$J = J_0 \left(e^{\frac{q(V-R_S J)}{nk_B T}} - 1 \right) + \frac{V - R_S J}{R_{Sh}} - J_{ph} \tag{24}$$

Where J_0, J_{ph}, R_s, R_{sh}, q, n, k_B and T are the saturation current density, the photocurrent density, the series resistance, the shunt resistance, the electron charge, the ideality factor, the Boltzmann constant and the temperature, respectively. By fitting the Shockley equation (Fig. 9), the estimated parameters are extracted and listed in Table 1. It is shown that R_s of the device with the cathode confinement in the thermal treatment is greatly reduced compared to the device without the cathode confinement in the thermal treatment (from 9.34 Ωcm² to 4.43 Ωcm²). R_s can significantly affect the device performance and reducing the value of R_s is an efficient method to increase *PCE*. The reduced R_s by using the cathode confinement plays one main role for the significant performance improvement of polymer solar cells. R_s is directly related to the contacts between the cathode and the active layer. Thus, these contacts were addressed by the XPS measurement.

The interfacial analysis results obtained by XPS measurement are shown in Fig. 10. Each top curve and bottom curve in the Al 2p, C 1s, O 1s and S 2p core level spectra graphs are corresponding to the samples with and without cathode confinement in the thermal treatment. As shown in Fig. 10, both samples show the Al 2p spectrum peaks located at the binding energy (BE) of 74.95 eV and 74.6 eV, which are corresponding to the Al oxide and Al-O-C bond, respectively, by referring to Table 2. The Al-O-C bond is also confirmed by the peaks located at the BE of 286.2 eV in the C 1s spectrum and 531 eV in the O 1s spectrum as

shown in Fig. 10. It has indicated that the Al-O-C bond is formed by the reaction of Al atoms and the carbonyl groups in PCBM and its existence will improve the contact between the polymer and the metal for both samples. However, by using the cathode confinement in thermal treatment, there is an additional shoulder peak at the BE of 76 eV in the Al 2p spectrum, which means that there forms an additional chemical bond. The additional chemical bond signal can also be seen from the S 2p spectrum. Although the typical peaks of P3HT appeared at the BE of 164.1 eV ($2p_{3/2}$) and 165.3 eV ($2p_{1/2}$) due to the spin-orbit coupling are observed for both samples in S 2p spectrum, there is an extra shoulder peak at the BE of 162.4 eV for the sample by using the cathode confinement. Considering the donation of electron density from the Al metal to the thiophene ring of P3HT, these additional peaks suggest that the interaction between P3HT and the Al metal occurs by using the cathode confinement in the thermal treatment.

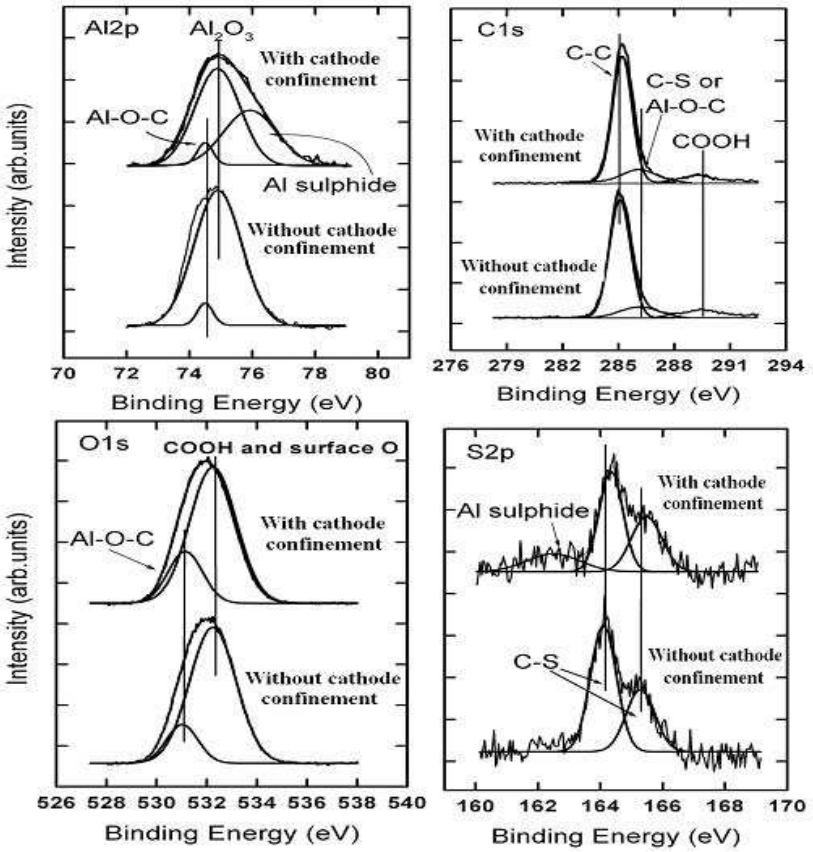

Fig. 10. High-resolution Al 2p, C 1s, O 1s and S 2p XPS spectra of the samples without (bottom curve) and with (top curve) the cathode confinement in the thermal treatment. The samples have the configuration of ITO/P3HT:PCBM (100 nm)/ Al(3 nm). By using the cathode confinement, there is an additional shoulder peak at the BE of 76 eV in the Al 2p spectrum and an additional shoulder peak at the BE of 162.4 eV in the S 2p spectrum.

Bonding states	Al 2p (eV)	C 1s (eV)	O 1s (eV)	S 2p (eV)
Al-O-C	74.6	286.2	531	
Al_2O_3	74.95		532.3	
Al-S	76			162.4
COOH		289.5		
C-C		285.1		
C-S		285.7		164.1, 165.3

Table 2. Summary of the XPS Binding Energies of Different Bonding States

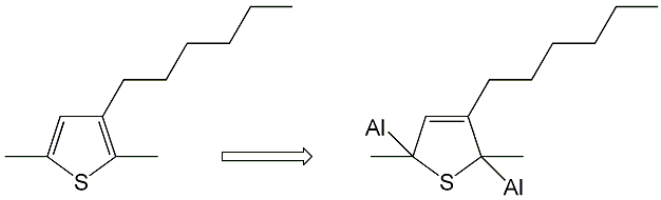

Fig. 11. The proposed molecular structure transits from P3HT to P3HT-Al complex.

Since the direct reaction between the Al atoms and the sulfur atoms is unlikely to occur because of the inherently high electron density on these sites, it is suggested that the Al atoms form bonds with the carbon atoms on the thiophene ring in the positions adjacent to the sulfur atom and form the P3HT-Al complex. One possible structure of the P3HT-Al complex is proposed in Fig. 11. The formation of the P3HT-Al complex will change the electron density of the sulfur atoms. In the P3HT-Al complex, the overall charge density of the sulfur atoms is smaller than that of the pristine P3HT. Thus the S 2p peaks located at the BE of 164.1 eV and 165.3 eV are shifted to the higher BE side at 164.3 eV and 165.5 eV, respectively, for the sample with the cathode confinement in the thermal treatment. Although the P3HT-Al complex is formed, there is only a slight energy difference (~0.1 eV shift in BE) in the C 1s spectrum for both samples as shown in Fig. 10. This is because the C 1s peak is dominated by the aliphatic carbon atoms while the Al atoms preferentially react with the carbon atoms in the conjugated system (thiophene ring of P3HT in this case). The signal arose from the interaction between P3HT and Al is too weak to affect the C 1s spectrum of the sample with cathode confinement. This explains why only very small energy difference in the C 1s spectrum is observed. The exact structure of P3HT-Al complex needs to be ascertained by further experiments.

It has been reported that Al metal can effectively transfer the electron to the conjugated polymer with the sulfide species and this feature makes it as a potential cathode for polymer electronics [Ling et al., 2002]. Another study [Reeja-Jayan et al., 2010] also has reported that Cu can react with P3HT and form sulfide-like species. The formed sulfide-like species can improve the solar cell performance. It is believed that the formation of the P3HT-Al complexes will play the same role. With the help of P3HT-Al complexes and the Al-O-C bonds, there is a better contact between the electrode and the active layer. This improved contact effectively reduces R_s and results in the improvement of the device performance.

How R_s affects the device performance is clearly shown in Fig. 12. It is shown that a large R_s will induce the decrease of *FF* and J_{SC}. By reducing R_s, *FF* and J_{SC} are increased and thus the

device performance is improved. At the same time, it is also noted that although both *FF* and J_{SC} can be affected by R_s, their dependences on R_s are different. From Fig. 12, it can be seen that *FF* can be greatly adjusted by R_s when the value of R_s is just larger than 1.0 Ωcm². The decrease of R_s from 9.34 Ωcm² to 4.43 Ωcm² (Table 1) should be the main reason for the increase of *FF* from 57.13% to 62.25% (Table 1) for the sample by using the cathode confinement. However, there is no obvious change of J_{SC} observed until R_s is larger than 25 Ωcm² (Fig. 12). Since R_s of the two devices are relative low (9.34 Ωcm² and 4.43 Ωcm² respectively, Table 1), it seems that the decrease of R_s is not the main reason for the obvious increase of J_{SC} (from 7.50 mA/cm² to 8.34 mA/cm², Table 1) by using the cathode confinement. This conclusion is also confirmed by the extracted parameter of J_{ph}. J_{ph} is mainly determined by the properties of the active layer and only slightly depends on R_s (independent parameters in equation (24)). If the cathode confinement in the thermal treatment is only to improve the contact and reduce R_s, there should be no such obvious change of J_{ph} (from 7.62 mA/cm² to 8.40 mA/cm², Tabel I). Thus, there must be other more important factors besides R_s which lead to the obvious increase of J_{ph}. It is well known that J_{ph} is very sensitive to the device morphology and material absorption, and thus these aspects should be well addressed.

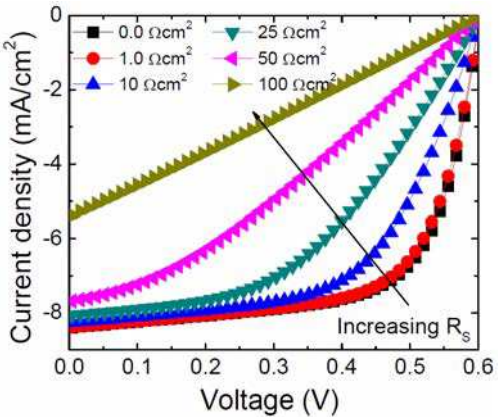

Fig. 12. Effect of R_s variation on *J–V* characteristics of the P3HT:PCBM solar cells according to (1). Only the value of R_s is changed while keep J_0=3.03e-5 mA/cm², J_{ph} =8.40 mA/cm², R_{sh} =617.28Ω cm² and n= 1.88. R_s greatly affects *FF* and thus the overall *PCE*. J_0, R_{sh} and n only slightly affect J_{SC} in the value range shown in Table 1.

The effects of cathode confinement on the device morphology are firstly investigated by the AFM measurement. Because the interface between the active layer and the cathode is mainly enriched by PCBM upon thermal treatment, the evolution of the surface morphology directly reflects the change of the PCBM domains. As shown in Fig. 13, it is shown that the thermal treatment effectively leads to the growth of the PCBM domains and thus increases the root mean square roughness. However, comparing to the device without the cathode confinement, there is a smoother surface morphology for the device with the cathode confinement. As shown in the AFM phase images (Fig. 13 b and c), there is a smaller island size for the sample with the cathode confinement. The profile measurements (Fig. 13 e and f) also show that the average peak-to-peak height and the width of the surface morphology are reduced by 20% and 33% by using the cathode confinement. Since surface morphology change is mainly induced

by the aggregates of PCBM, the smoother surface morphology means that the cathode confinement can prevent the formation of too large underlying PCBM domains.

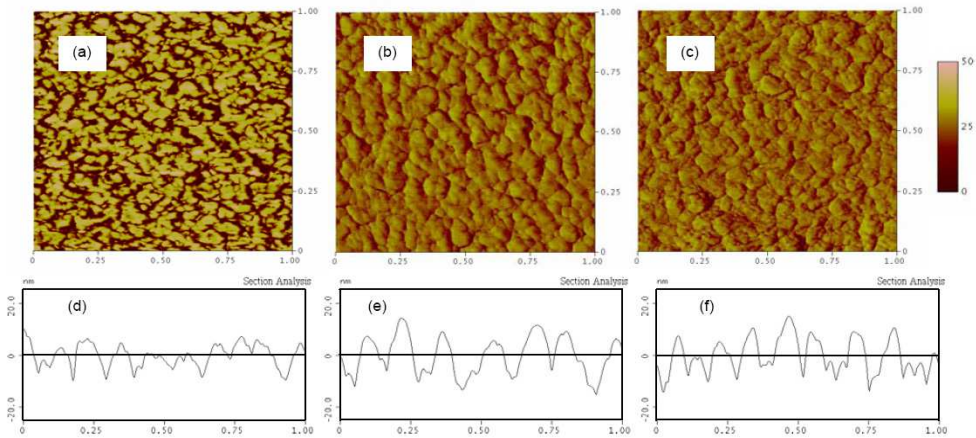

Fig. 13. Tapping-mode AFM phase images of Al covered P3HT:PCBM blend film: (a) sample without any thermal treatment and samples without (b) and with (c) the cathode confinement in the thermal treatment. Their corresponding cross sectional profiles are shown in (d) to (f) with root mean square roughness 5.5, 6.3 and 5.9 nm respectively.

It is well known that the main roles of annealing process are to induce the redistribution of PCBM and increase the crystallization of P3HT, so that the bicontinuous interpenetrating networks is achieved and meanwhile the optical absorption capability is enhanced. However, a too fast PCBM diffusion will lead to the formation of very large PCBM aggregates and thus destroy the optimal bicontinuous interpenetrating network. Besides, too large PCBM domains also reduce the interfacial contact area between P3HT and PCBM and lead to the inefficient exciton dissociation. In order to achieve a high performance, it is required to well control the PCBM domain size. It is shown here that the overgrowth of the PCBM domains in the thermal treatment is effectively inhibited by using the cathode confinement. Thus a better nanoscale morphology control is achieved. Similar metal confinement effect was also demonstrated on the organic surface by using silver cap [Peumans et al., 2003]. The improved morphology will decrease the exciton loss, facilitate the charger transport and thus increase J_{SC}.

J_{SC} is also directly related to the optical absorption of the active layer. In order to investigate the effects of cathode confinement on the optical absorption capability, the UV-Vis absorption spectra of the active layer capped with the Al electrode were measured. Because the annealed metal results in a slight variation of the light absorption, the optical spectra were obtained by subtracting the pure metal spectra. The results are shown in Fig. 14. All the samples show the typical absorption spectrum of P3HT:PCBM blend film with the absorption peak at the wavelength of 515 nm and shoulders at 550 nm and 604 nm. The thermal treatment obviously increases the optical absorption of the P3HT:PCBM film. However, there is a better optical absorption capability for the sample with the cathode confinement (e in Fig. 14) compared to the sample without the cathode confinement (d in Fig. 14). It is well known that the absorption capability of P3HT:PCBM system is directly related to the P3HT crystallites. The crystallization of P3HT was measured by XRD.

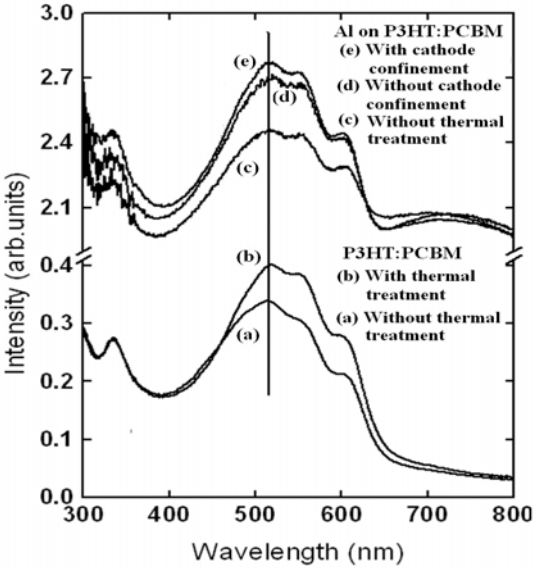

Fig. 14. Optical absorption spectra of various samples: (a) bare P3HT:PCBM blend film without thermal treatment (b) bare P3HT:PCBM blend film with thermal treatment (c) Al covered P3HT:PCBM blend film without the thermal treatment (d) Al covered P3HT:PCBM blend film with the thermal treatment done before cathode deposition (e) Al covered P3HT:PCBM blend film with the thermal treatment done after cathode deposition.

Fig. 15 shows the obtained XRD measurement results. A characteristic peak around $2\theta = 5.4°$ is observed for all the samples, which is associated with the lamella structure of thiophene rings in P3HT. Based on Bragg's law and Scherrer relation, the lattice constant (d) and the size of the polymer crystallites (L) can be determined:

$$n\lambda = 2d\sin\theta \tag{25}$$

$$L = \frac{0.9\lambda}{\Delta_{2\theta}\cos\theta} \tag{26}$$

where λ is the wavelength of the x-ray, θ the Bragg's angle, $\Delta_{2\theta}$ the smallest full width at half maximum of the peak. The extracted d and L are listed in Table 3. It is shown that all the samples show the lattice constant of 1.62 ± 0.01 nm that represents the P3HT crystallites in a-axis orientation. Thermal treatment increases the crystallization of P3HT. However, the increased magnitudes are different for the devices with and without the cathode confinement. The sample with the help of the cathode confinement in the thermal treatment shows the highest peak. As listed in Table 3, the size of the P3HT crystallites (L value of 17.7 nm) is increased by 36% by using the cathode confinement compared to without the cathode confinement (L value of 13 nm). The increased crystallite size may come from the effective inhibition of the strong PCBM diffusion by the cathode confinement. It has been shown [Swinnen et al., 2006] that a too strong diffusion of PCBM from the P3HT matrix would reduce the P3HT crystallization and optical absorption property. Because of the presence of

the cathode in the thermal treatment, the PCBM diffusion is slowed down. Thus it is easier for P3HT to be crystallized. The increased P3HT crystallites will enhance the active layer optical absorption capability and increase J_{SC}.

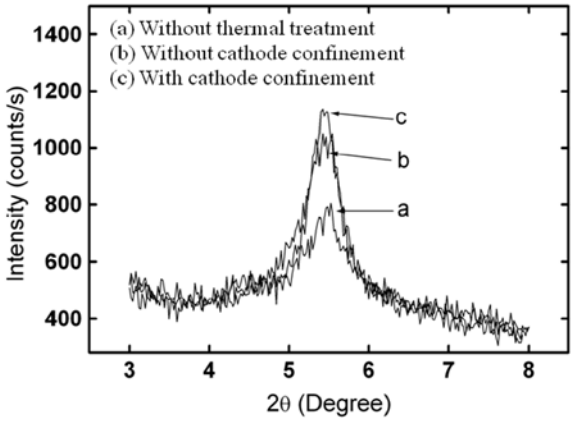

Fig. 15. X-ray diffraction spectra of various samples: (a) Al covered P3HT:PCBM blend film without the thermal treatment (b) Al covered P3HT:PCBM blend film with the thermal treatment done before cathode deposition (c) Al covered P3HT:PCBM blend film with the thermal treatment done after cathode deposition.

Samples	2θ [°]	$\Delta_{2\theta}$ [°]	h [counts/s]	L [nm]	d [nm]
Without thermal treatment	5.49	0.83	318	9.6	1.61
Without cathode confinement	5.44	0.61	596	13	1.625
With cathode confinement	5.44	0.45	617	17.7	1.625

Table 3. Summary of X-Ray Diffraction Peaks of P3HT:PCBM from Fig.15

3.3 Summary

P3HT:PCBM solar cells with the cathode confinement in the thermal treatment show better performance than the solar cells without the cathode confinement in the thermal treatment. The effects of the cathode confinement on the device performance have been investigated in this work. According to the XPS results, it is found that the Al-O-C bonds and P3HT-Al complexes are formed at the interface between the active layer and the cathode by using the cathode confinement. These chemical structures effectively reduce the contact resistance and improve the device performance. More importantly, the cathode confinement effectively improves the active layer morphology. According to the AFM, UV-Vis absorption spectra and XRD measurement results, it is found that the cathode confinement in the thermal treatment not only prevents the overgrowth of the PCBM domains, but also increases the crystallization of P3HT. With the help of cathode confinement in the thermal treatment, a better optical absorption and a more ideal bicontinuous interpenetrating networks can be obtained at the same time. This will effectively reduce the exciton loss and improve the charge transport capability. Thus an improved device performance is achieved.

4. Overall optimization of polymer solar cells

Because the active layer is very thin in compared with the incident light wavelength, the optical interference effect influences the absorption and J_{SC} as discussed in above. According to the simulated results based on the optical model, the thickness will be optimized around the first and second optical interference peaks in this part. In addition, the annealing process can efficiently improve the performance of P3HT:PCBM polymer solar cells. The performance is related to the annealing sequence, and post-annealing is more favored by the devices. Based on this conclusion, all the polymer solar cells were fabricated and post-annealed in this section. These devices were used to optimize the overall solar cell performance.

4.1 Experimental

The fabrication process is the same as above. The devices were fabricated on the ITO-coated glass substrates. After routine solvent cleaning (treated sequentially with detergent, de-ionized water, acetone, and isopropanol in an ultrasonic bath for about 15 minutes), the dried ITO glass substrates were treated with oxygen plasma for about three mins. Then the filtered PEDOT:PSS suspension was spin coated on the top of the ITO surface under ambient condition. The P3HT:PCBM solution dissolved in dichlorobenzene with a weight ratio of 1:0.8 was spin coated in the glove box. Finally, Al cathode was deposited by e-beam evaporation through a shadow mask. All the devices have same structure: ITO\PEDOT:PSS\P3HT:PCBM\Al, and only the thicknesses of the P3HT:PCBM active layers are different. The active layer thickness was controlled by changing the spin speed and solution concentration. Then different annealing temperatures are tested for the devices based on post-annealing to find the optimized conditions. The *J-V* characteristics were measured using a Keithley 2400 parameter analyzer in the dark and under a simulated light intensity of 100 mW/cm^2 (AM 1.5G) calibrated by an optical power meter.

4.2 Experimental results and discussion

4.2.1 Optical interference effects and active layer thickness optimization

The TMF method as discussed in section 2 is used to predict J_{SC} for the active layer thickness in a range from 50 nm to 250 nm for 1:0.8 P3HT:PCBM active layer. The results are plotted in Fig. 16. As predicted, obvious polymer solar oscillatory behavior is observed because of the very thin active layer compared with the light wavelength. When the P3HT:PCBM ratio is 1:0.8, the first and second optical interference peaks are found at the P3HT:PCBM layer thicknesses of around 85 nm and 230 nm. Both the two optical interference peaks should be used to optimize the active layer thickness.

According to the simulated results, the devices were fabricated around the first and the second optical interference peaks. The experimental results for the different active layer thicknesses are shown Fig. 17. As predicted, J_{SC} shows a periodic behavior with the variation of the active layer thickness. The J_{SC} increases from as low as 6.25 mA/cm^2 (for the device with active layer thickness, t=64 nm) to as high as 6.93 mA/cm^2 (for t=80 nm), and then decreases around the first interference peak. The same trend is observed around the second optical interference peak at a thickness of 208 nm. J_{SC} reaches a value as high as 10.37 mA/cm^2 at the second optical interference peak. The higher J_{SC} comes from the better absorption ability. It is obviously shown that the second peak can absorb more light than the first peak as shown in Fig. 18. Thus the second optical interference peak is more preferred to achieve a higher *PCE*. Then around this peak, the annealing conditions are investigated.

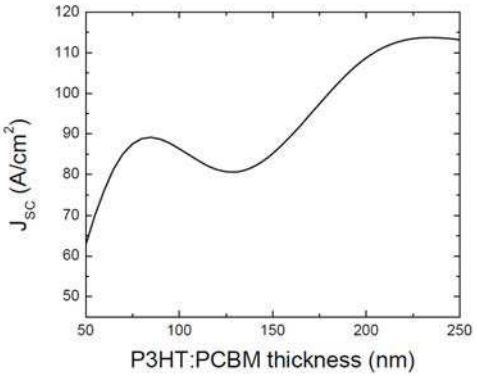

Fig. 16. J_{SC} versus P3HT:PCBM thickness, P3HT:PCBM with weight ratio of 1:0.8 and device structure of ITO/PEDOT:PSS/P3HT:PCBM/Al.

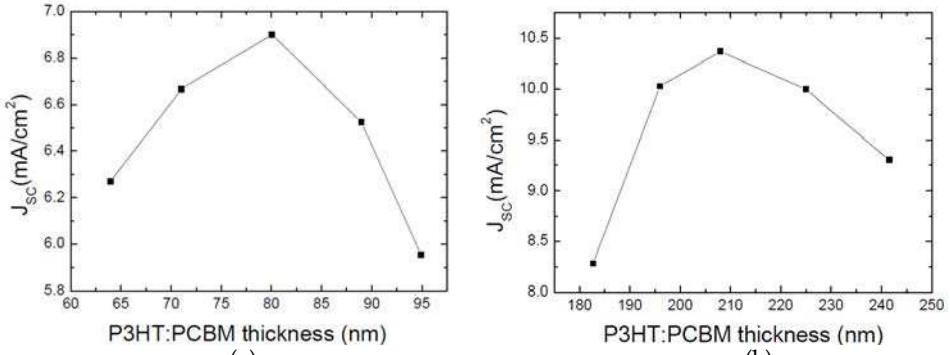

Fig. 17. Optimization of active layer thickness. (a) around the first optical interference peak, and (b) around the second optical interference peak. All devices were post-annealed at 160^{o}C for 10 mins.

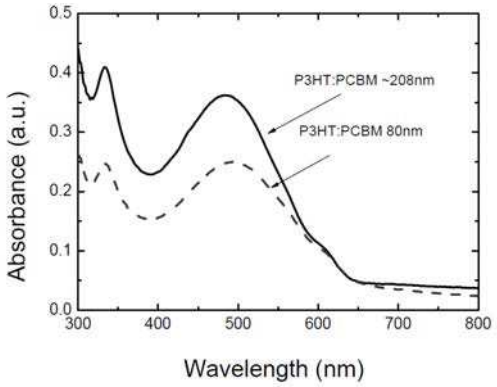

Fig. 18. UV-visible absorption spectra of P3HT:PCBM (about 80 nm thick and 208 nm thick).

4.2.2 Optimization of annealing conditions

The device performance depends greatly on annealing temperatures as clearly seen from Fig. 19. The reasons for the performance to be improved by the annealing process have been widely investigated and discussed in section 3. It is clear that for an efficient bulk HJ polymer solar cell, *D* and *A* domains must be small enough so that most of the excitons can diffuse into the *D/A* interfaces before they decay. At the same time, the interpenetrating transport network must be formed for the efficient charge transport. Thus, the morphology optimization is of great important. By varying the annealing condition, the morphology can be well controlled.

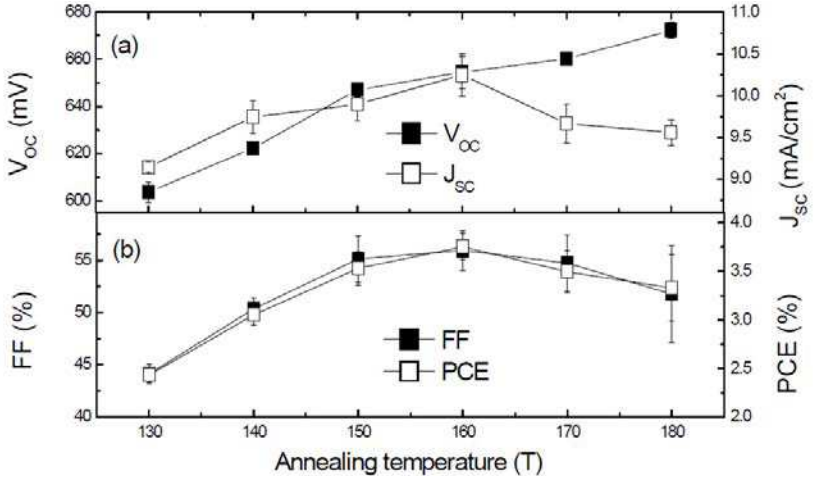

Fig. 19. (a) and (b): Relations of device performance and annealing conditions. The P3HT:PCBM layer thickness keeps constant of 208 nm.

These results were related to the better morphology as discussed in previous and also related to the increase of the charge carrier mobility. The same reason should also be responsible for our results. The highest *PCE* in our experiments is achieved when the annealing temperature is 160°C which is very close to the annealing temperatures reported by Ma (Ma et al., 2005). The analysis of changes in film morphology has shown that the changes in film crystallinity and aggregation within the film PCBM nanophase lead to the improved solar characteristics at this temperature. When the annealing temperature is increased, a steady enhancement of V_{OC} is observed because the e-beam evaporated Al can induce dipoles at the interface between active layer and cathode [Zhang et al., 2009]. As shown in Fig. 19, the device shows the optimized performance when it has been annealed at 160°C for 10 min.

5. Conclusion

In polymer solar cells, because of the optical interference effect, the total exciton generation rate does not increase monotonically with the increase of the active layer thickness, but behaves wave-like, which induces the corresponding variation of J_{SC}. The carrier lifetime also inffuence J_{SC} greatly. When the carrier lifetime is long enough, dissociation probability will play a very important role for a thicker active layer. J_{SC} will behave wave-like with the variation of active layer thickness. When the carrier lifetime is too short (drift length is

smaller than device thickness), accumulation of charges will appear near the electrode and J_{SC} will increase at the initial stage and then decrease rapidly with the increase of active layer thickness.

The experimental studies were carried out to investigate P3HT:PCBM based HJ polymer solar cells in this chapter. It was found that the strengthened contact due to the bonding reinforcements (Al-O-C bonds and P3HT-Al complex) at the active layer/metal interface for post-annealed device improves the charge collection at the cathode side. Carrier separation can be facilitated via the improved nanoscaled morphology of the post-annealed polymer blend. The Al capping layer promotes efficient formation of the P3HT crystallites and thus enhances the light harvesting property of the polymer blend. Evidence for the latter has been derived from the improved shape of the absorption spectrum. The results underline the importance of applying the most efficient annealing sequence in order to achieve the best solar device performance.

Based on above results, the overall performance of P3HT:PCBM bulk polymer solar cells were optimized. As predicted by the TMF method, an obvious polymer solar cell oscillatory behavior of J_{SC} was observed in the experiments. The devices were optimized around the first two optical interference peaks. It was found that the optimized thicknesses are 80 nm and 208 nm. Based on the post-annealing, different annealing temperatures have been tested. The optimized annealing condition was found to be 160^{o}C for 10 min in a nitrogen atmosphere.

6. References

Cheyns, D.; Poortmans, J.; Heremans, P.; Deibel, C.; Verlaak, S., Rand, B. P. & Genoe J. (2008). Analytical model for the open-circuit voltage and its associated resistance in organic planar heterojunction solar cells. *Physical Review B*, Vol. 77, No. 16, (April 2008), pp. 165332-1–165332-10, ISSN 1098-0121

Goodman, A. M. & Rose, A. (1971). Double Extraction of uniformly generated electron-hole pairs from insulators with nonjecting contacts. *Journal of Appllied Physics.* Vol. 42, No. 7, (June 1971). pp. 2823-2830. ISSN 0021-8979

Kim, H. J.; Park, J. H.; Lee, H. H.; Lee D. R.; & Kim, J. J. (2009). The effect of Al electrodes on the nanostructure of poly(3-hexylthiophene): Fullerene solar cell blends during thermal annealing, organic electronics, Vol. 10, No. 8, (December 2009). pp. 1505-1510. ISSN 1566-1199

Koster, L. J. A.; Smits, E. C. P.; Mihailetchi, V. D. & Blom, P. W. M. Device model for the operation of polymer/fullerene bulk heterojunction solar cells. *Physical Review B*, Vol. 72, No. 8, (August 2005) pp. 085205-1-085205-9. ISSN 1098-0121

Lacic, S. & Inganas, O. (2005). Modeling electrical transport in blend heterojunction organic solar cells. *Journal of Applied Physics*, Vol. 97, No. 12, (June 2005). pp. 124901-1-124901-7. ISSN 0021-8979

Ma, W.; Yang, C.; Gong, X.; Lee, K. & Heeger, A. J. (2005). Thermally stable, efficient polymer solar cells with nanoscale control of the interpenetrating network morphology, Advacned Functional Materials, Vol. 15, No.10, (October 2005).1617-1622. ISSN 1616-301X

Li, G.; Shrotriya, V. & Yao Y. (2005). Investigation of annealing effects and film thickness dependence of polymer solar cells based on poly(3-hexylthiophene). *Journal of Appllied Physics.*Vol. 98, No. 4 (August 2005), pp. 43704-1-43704-5. ISSN 0021-8979

Ling, Q. D.; Li, S.; Kang, E. T.; Neoh, K. G.; Liu, B. & Huang, W. (2002). Interface formation between the Al electrode and poly[2,7-(9,9-dihexylfluorene)-*co*-alt-2,5-(decylthiophene)] (PFT) investigated in situ by XPS , *Applied Surface Science*, Vol. 199, No. 1-4, (October 2002). pp. 74-82.

Monestier, F.; Simon, J. J.; Torchio, P.; Escoubas, L.; Flory, F.; Bailly, S.; Bettignies, R.; Guillerez, S. & Defranoux, C., Modeling the short-circuit current density of polymer solar cells based on P3HT:PCBM blend. *Solar Energy Materials & Solar Cells*, Vol. 91, No. 5, (March 2007). pp. 405-410. ISSN 0927-0248

Mihailetchi, V. D.; Xie, H.; Boer，B.; Koster L. J. A. & Blom, P. W. M. Charge Transport and Photocurrent Generation in Poly(3-hexylthiophene): Methanofullerene Bulk-Heterojunction Solar Cells. *Advacned Functional Materials*, Vol. 16, No. 5, (March 2006). pp. 699-708. ISSN 1616-301X

Pettersson, L. A. A.; Roman, L. S. & Inganas, O. (1999). Modeling photocurrent action spectra of photovoltaic devices based on organic thin films. *Journal of Applied Physics*, Vol. 86, No. 1, (1999). pp. 487-496. ISSN 0021-8979

Peumans, P.; Yakimov, A. & Forrest, S. R. (2003). Small molecular weight organic thin-film photodetectors and solar cells. *Journal of Applied Physics*, Vol. 93, No. 7, (April 2003). pp. 3693-3723. ISSN 0021-8979

Peumans, P.; Uchida, S. & Forrest, S. R. (2003). Efficient bulk heterojunction photovoltaic cells using small-molecular-weight organic thin films, *Nature*, Vol. 425, No. 6954, (September 2003). pp. 158-162.

Reeja-Jayan, B. & Manthiram, A. (2010). Influence of polymer–metal interface on the photovoltaic properties and long-term stabilityofnc-TiO2-P3HT hybrid solar cells,Solar Energy Materials & Solar Cells, Vol. 94, No. 5, (February 2010). pp. 907-914. ISSN 0927-0248

Swinnen, A.; Haeldermans, I.; Ven, M. V.; Haen, J. D.; Vanhoyland, G.; Aresu, S.; Olieslaeger, M. D. & Manca, J. (2006). Tuning the dimensions of C_{60}-based needlike srystals in blended thin films , *Advacned Functional Materials*, Vol. 16, pp. 760-765, 2006. ISSN 1616-301X

Zhang, C. F.; Tong, S. W.; Jiang, C. Y.; Kang, E. T.; Chan, D. S. H. & Zhu, C. X. (2008). Efficient multilayer organic solar cells using the optical interference peak, Applied Physics Letters, Vol. 93, No. 4, (August 2008). pp. 043307-1-043307-3.ISSN 0003-6951

Zhang, C. F.; Tong, S. W.; Jiang, C. Y.; Kang, E. T.; Chan, D. S. H. &Zhu, C. X. (2009). Enhancement in open circuit voltage induced by deep interface hole trapsin polymer-fullerene bulk heterojunction solar cells. Applied Physics Letters, Vol. 94, No. 10, (March 2009). pp. 103305-1-103305-3. ISSN 0003-6951

Zhang, C. F.; Hao, Y.; Tong, S. W.; Lin, Z. H.; Feng, Q; Kang, E. T. & Zhu, C. X. (2011). Effects of Cathode Confinement on the Performance of Polymer/Fullerene Photovoltaic Cells in the Thermal Treatment, *IEEE Transaction on Electron Devices*, Vol. 58, No. 3, (March 2011), pp. 835-842. ISSN 0018-9383

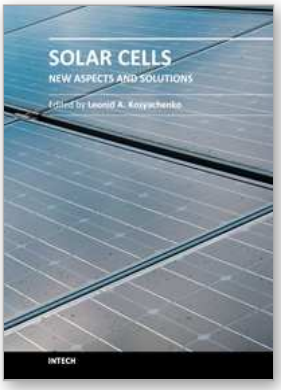

Solar Cells - New Aspects and Solutions

Edited by Prof. Leonid A. Kosyachenko

ISBN 978-953-307-761-1
Hard cover, 512 pages
Publisher InTech
Published online 02, November, 2011
Published in print edition November, 2011

The fourth book of the four-volume edition of 'Solar cells' consists chapters that are general in nature and not related specifically to the so-called photovoltaic generations, novel scientific ideas and technical solutions, which has not properly approved. General issues of the efficiency of solar cell and through hydrogen production in photoelectrochemical solar cell are discussed. Considerable attention is paid to the quantum-size effects in solar cells both in general and on specific examples of super-lattices, quantum dots, etc. New materials, such as cuprous oxide as an active material for solar cells, AlSb for use as an absorber layer in p-i-n junction solar cells, InGaAsN as a promising material for multi-junction tandem solar cells, InP in solar cells with MIS structures are discussed. Several chapters are devoted to the analysis of both status and perspective of organic photovoltaics such as polymer/fullerene solar cells, poly(p-phenylene-vinylene) derivatives, photovoltaic textiles, photovoltaic fibers, etc.

How to reference

In order to correctly reference this scholarly work, feel free to copy and paste the following:

Chunfu Zhang, Hailong You, Yue Hao, Zhenhua Lin and Chunxiang Zhu (2011). Effects of Optical Interference and Annealing on the Performance of Polymer/Fullerene Bulk Heterojunction Solar Cells, Solar Cells - New Aspects and Solutions, Prof. Leonid A. Kosyachenko (Ed.), ISBN: 978-953-307-761-1, InTech, Available from: http://www.intechopen.com/books/solar-cells-new-aspects-and-solutions/effects-of-optical-interference-and-annealing-on-the-performance-of-polymer-fullerene-bulk-heterojun

INTECH
open science | open minds

InTech Europe
University Campus STeP Ri
Slavka Krautzeka 83/A
51000 Rijeka, Croatia
Phone: +385 (51) 770 447
Fax: +385 (51) 686 166
www.intechopen.com

InTech China
Unit 405, Office Block, Hotel Equatorial Shanghai
No.65, Yan An Road (West), Shanghai, 200040, China
中国上海市延安西路65号上海国际贵都大饭店办公楼405单元
Phone: +86-21-62489820
Fax: +86-21-62489821